ChemComm

Accepted Manuscript

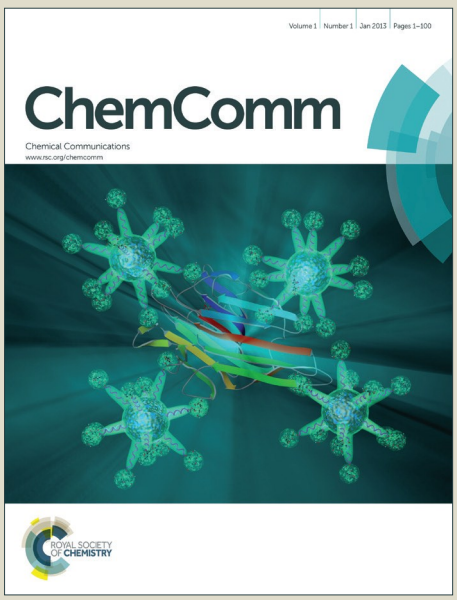

ROYAL SOCIETY OF CHEMISTRY

www.rsc.org/chemcomm

Journal Name

COMMUNICATION

Efficient Perovskite Solar Cell Fabricated Using an Aqueous Lead Nitrate Precursor

Received 00th January 20xx,
Accepted 00th January 20xx

DOI: 10.1039/x0xx00000x

www.rsc.org/

Tsung Yu Hsieh,[a] Tzu-Chien Wei,[a*] Kuan-Lin Wu,[b] Masashi Ikegami,[b] and Tsutomu Miyasaka[b]

A novel, aqueous precursor system ($Pb(NO_3)_2$ + water) is developed to replace conventional (PbI_2 + DMF) for fabricating methylammonium lead iodide ($MAPbI_3$) perovskite solar cells (PSC). When the morphology and surface coverage of the $Pb(NO_3)_2$ film was controlled during coating, a power conversion efficiency of 12.58% under a standard condition (AM1.5, 100 mW/cm^2) was achieved for the PSC.

Inorganic-organic lead halide perovskite crystals possess a superior light absorption capability[1] and tuneable bandgap[2], rendering them promising for use in organic semiconductors[3], photo-detectors,[4] and photovoltaics[1, 5]. The goal of using methylammonium lead iodide perovskite ($MAPbI_3$) as a light harvester for organic photovoltaics began in 2009, when Miyasaka et al. fabricated the first $MAPbX_3$ (X = Br or I)-sensitized solar cells by using a liquid electrolyte[1]. However, liquid electrolytes are corrosive against perovskite crystals and were replaced by solid-state hole conductors, which improve power conversion efficiency (PCE) and device stability[5]. To date, a certified PCE of perovskite solar cells (PSCs) exceeding 20% has been achieved.

One of the advantages of PSCs is that although their architecture is versatile, they can be fabricated using cost-effective and scalable solution processes[5-10]. In general, $MAPbI_3$ crystals, the product of a lead-containing precursor and methylammonium iodide (MAI), are formed through one-step[6, 11] or sequential deposition[12-14], depending on whether the lead source and MAI are deposited onto the substrate once or sequentially. $MAPbI_3$ is the most explored perovskite material, and various lead-containing precursors such as lead iodide (PbI_2)[12, 13, 15], lead chloride[6, 16], lead acetate[17, 18], hydroiodized lead iodide[19], lead acetylacetone[18], and lead thiocyanate[20] have also been studied. PbI_2 is the basic material used in preparing $MAPbI_3$, because it contains lead as well as iodide. Although the photovoltaic performance yielded by different lead precursors varies, almost all studies have used high polarity, aprotic solvents such as dimethylformamide (DMF) because of the solubility.

Concerns regarding the toxicity of PSCs have been addressed recently[21]; organo-lead compounds are severely harmful to the human body and the environment. Therefore, research on creating lead-free PSCs is intensive[22-25]. While most debate addresses on the hazard of organo-lead in perovskite crystals, in this paper, we propose concerns regarding the processing solvent used during perovskite deposition. Compared with lead perovskite, the pathology of which is uncertain, DMF is a toxicant and has been linked to liver disease clinically[26, 27]. Herein, we report our first attempt to fabricate highly efficient PSCs by using a water-based lead-precursor, lead nitrate ($Pb(NO_3)_2$), and sequential deposition[12]. The $Pb(NO_3)_2$ was combined with water, and the surface morphology and formation of the perovskite structure were carefully scrutinised using scanning electron microscopy (SEM) and X-ray diffraction (XRD). The $Pb(NO_3)_2$/water system is an alternative system that can be used in PSCs without the need for toxic solvents. During current optimisation, a PCE of 12.58% was achieved under standard test condition (AM1.5, 100 mW/cm^2).

Figure 1 shows a schematic diagram of the device architecture and the process for fabricating perovskite layers in the $Pb(NO_3)_2$/water system. The device architecture (Fig. 1a) features a bilayer structure comprising a blocking (BL) TiO_2 layer and a mesoporous TiO_2 scaffold, which benefits charge collection and hysteresis minimisation[11, 28]. The perovskite layer was prepared using sequential deposition, primarily according to the process described in a published report[12]; however, the PbI_2/DMF precursor solution was replaced by an aqueous $Pb(NO_3)_2$ solution. The process we used (Fig. 1b) involves additional UV-ozone pre-treatment on the mesoporous TiO_2-containing substrate before $Pb(NO_3)_2$ spin-coating to enhance wettability between the mesoporous TiO_2 and hydrophilic $Pb(NO_3)_2$. Fig. 1c shows an XRD analysis of the resulting perovskite film. The conversion of $Pb(NO_3)_2$ to $MAPbI_3$ by using DMF as processing solvent has been confirmed in previous studies[18, 28, 29]; our results further reveal that perovskite crystals can be formed in an aqueous $Pb(NO_3)_2$ solution. According to Fig. 1c, diffraction peak at 2θ = 14.2°, 28.5°, and 31.9° correspond to the (110), (220), and

[a] Department of Chemical Engineering, National Tsing-Hua University, Taiwan.
[b] Graduate School of Engineering, Toin University of Yokohama, Japan.

† Electronic Supplementary Information (ESI) available: Details information about the synthesis of MAI, device fabrication, characterization and other experimental data mentioned in main text. See DOI: 10.1039/x0xx00000x

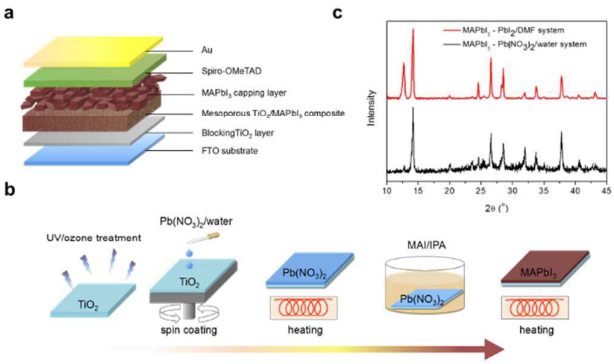

Fig. 1 Device architecture, scheme of perovskite layer fabrication process and XRD analysis of MAPbI3. a, Device architecture of PSC (FTO/TiO_2 blocking layer/mesoporous TiO_2-$MAPbI_3$ composite layer/$MAPbI_3$ capping layer/spiro-OMeTAD/Au). b, Procedure for preparing $MAPbI_3$ layer in the $Pb(NO_3)_2$/water system. c, XRD pattern of $MAPbI_3$ coated on FTO/blocking-TiO_2/mesoporous-TiO_2 substrate in the PbI_2/DMF and $Pb(NO_3)_2$/water system. The PbI_2 crystal was indexed as (001) at 2θ = 12.7° and the CH3NH3PbI3 crystal was indexed as (110), (220), and (312) at 2θ = 14.2°, 28.5°, and 31.9°, respectively.

(312) lattice planes of the perovskite, respectively. The diffraction peak at 12.7°, which is commonly found in a PbI_2/DMF system and represents the incomplete conversion of PbI_2 to $MAPbI_3$, becomes extremely weak in the $Pb(NO_3)_2$/water system, indicating the inherent advantage of a higher conversion of lead precursor and a purer perovskite crystal in the $Pb(NO_3)_2$/water system. Another feature apparent in the XRD results for the $Pb(NO_3)_2$/water system is that the peak intensity at 31.9° is relatively higher than that in the PbI_2/DMF system. This higher intensity may be attributed to the preferred orientation of crystal growth, which was altered in the $Pb(NO_3)_2$/water system. However, how it affects the photovoltaic property of perovskite crystal remains unknown and warrants investigation.

Notably, during the preparation of the perovskite layer in a $Pb(NO_3)_2$/water system, care must be taken in the spin-coating step. The morphology of $Pb(NO_3)_2$ strongly depends on the wettability between the hydrophilic $Pb(NO_3)_2$ and the TiO_2 scaffold. Figure 2 shows the SEM topographies of the samples after aqueous $Pb(NO_3)_2$ was spin-coated onto a TiO_2 scaffold. Without treatment on the surface before spin-coating, the resultant film has an extremely coarse, uneven morphology. Apparent in Fig. 2a, large grains with radial lines were exhibited on the mesoporous TiO_2 surface, indicating that most of the precursor solution was dispersed by centrifugal force during spinning. This pattern is generally regarded as the result of poor wettability between the film and the substrate. Thus, we applied a pre-treatment by exposing the TiO_2 scaffold-containing substrate to UV-ozone irradiation before spin-coating. The purpose of this treatment is to hydrophilize the surface, thereby improving the wettability before spinning. The change in the hydrophilicity of the TiO_2 substrate was investigated by measuring the water contact angle of the TiO_2 scaffold-containing substrate. According to the inset of Fig. 2a and Fig. 2b, the water contact angle decreased from 22.2° to 3.7° after UV-ozone treatment for 10 minutes. Because of the super hydrophilic surface, the morphology of the resultant $Pb(NO_3)_2$ changed dramatically. Fig. 2c is the zoom-in image of the central

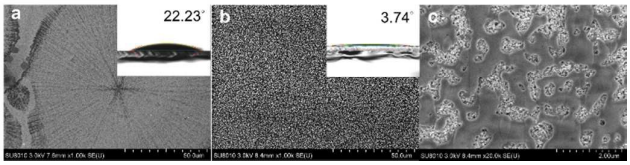

area in Fig. 2b. It can be seen in Fig. 2c an islandish film predominated the morphology of the $Pb(NO_3)_2$ (Fig. 2b).

Fig. 2 SEM topographies of $Pb(NO_3)_2$ on mesoporous-TiO_2. a, Without UV treatment before spin-coating aqueous $Pb(NO_3)_2$. b, With UV treatment before spin-coating aqueous $Pb(NO_3)_2$. c, High magnification of b. The inset shows the contact angle between the $Pb(NO_3)_2$ droplet and the mesoporous-TiO_2 layer.

Although large areas bare of TiO_2 remained, the $Pb(NO_3)_2$ was thoroughly distributed over an extensive area, and we thus presumed that infiltration to the inner porous structure of the TiO_2 scaffold was attributable to favourable wettability.

As noted previously, the XRD patterns of $MAPbI_3$ fabricated using an aqueous $Pb(NO_3)_2$ precursor revealed no PbI_2 residue, a phenomenon that prompted us to investigate the formation mechanism of such $MAPbI_3$. Shown in Fig. S1, according to the UV-vis spectra of the $Pb(NO_3)_2$-coated substrate dipped into an MAI solution for different durations, the conversion of $MAPbI_3$ from the $Pb(NO_3)_2$/water system required at least 200 seconds. Compared with the formation of $MAPbI_3$ in the PbI_2/DMF system, which reportedly requires only a few seconds for conversion from PbI_2[13], the formation of $MAPbI_3$ in our $Pb(NO_3)_2$/water system is much slower. To investigate the formation of $MAPbI_3$, the time-trajectory XRD pattern and corresponding SEM topography were monitored on the spin-coated $Pb(NO_3)_2$ film according to different MAI incubation times; Fig. 3 shows a summary of the results. According to Fig. 3a, before MAI incubation, diffraction peaks of pristine $Pb(NO_3)_2$ were found at 2θ = 19.6° and 22.7°. After a fluoride-doped tin oxide (FTO)/TiO_2/$Pb(NO_3)_2$ substrate was immersed in an MAI solution for 100 seconds (red line), the XRD features of the $Pb(NO_3)_2$ vanished and a new signal at 2θ = 12.7° indicated PbI_2 formation. When the incubation time increased, the diffraction peaks at 2θ = 12.7° gradually decreased and new diffraction peak at 2θ = 14.2° gradually increased, indicating the formation of the $MAPbI_3$ phase.

On the basis of XRD observation, we propose that the formation of $MAPbI_3$ from $Pb(NO_3)_2$ involves a two-step reaction:

$$Pb(NO_3)_2 + 2MAI \rightarrow PbI_2 + 2MANO_3 \quad (1)$$

$$PbI_2 + MAI \rightarrow MAPbI_3 \quad (2)$$

The first step is the formation of PbI_2, during which time $Pb(NO_3)_2$ is exposed to the MAI solution (reaction 1). Indicated as a red line of Fig. 3a, this reaction was rapidly completed within 100 seconds, and the characteristic peaks of pristine $Pb(NO_3)_2$ disappeared entirely, leaving only the characteristic peaks of PbI_2. Interestingly, no characteristic peaks representing $MAPbI_3$ are apparent on the red line, indicating that $MAPbI_3$ cannot be formed directly from $Pb(NO_3)_2$. In contrast to reaction 1, reaction 2, the transformation of PbI_2 to $MAPbI_3$, is much slower. Compared with reaction 1, which occurs within 100 seconds, reaction 2 requires approximately 700 seconds to entirely consume the PbI_2 formed from reaction 1. Compared with in a conventional PbI_2/DMF system, the

propagation and crystal growth of $MAPbI_3$ can be completed within few seconds[13]. Our results suggest that reaction 1 plays an important role to the kinetics

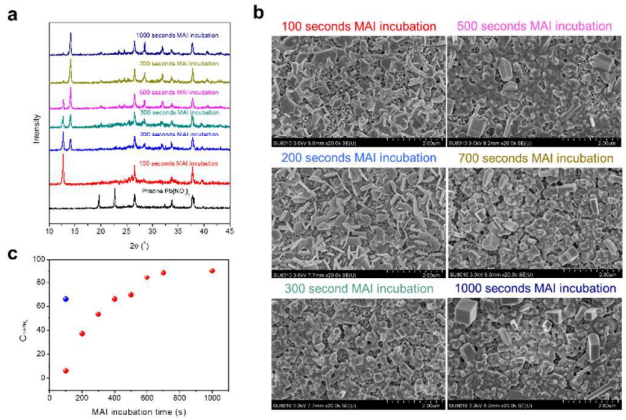

Fig. 3 XRD spectra and SEM images of $Pb(NO_3)_2$ film incubated in MAI for various durations. a, XRD spectra of FTO/blocking-TiO_2/mesoporous TiO_2-$Pb(NO_3)_2$ substrates immersing in MAI solution for sequential durations. b, SEM topographies of FTO/blocking TiO_2/mesoporous TiO_2-$Pb(NO_3)_2$ substrate immersed in MAI solution for sequential durations. c, Correlation between perovskite conversion and MAI incubation time in $Pb(NO_3)_2$/water system. The blue dot represents the conversion of perovskite in the PbI_2/DMF system; MAI incubation duration was fixed at 100 seconds.

of reaction 2, and the consumption of MAI in reaction 1 may account for this; however, such consumption requires further investigation.

Despite the slow rate of $MAPbI_3$ formation in the $Pb(NO_3)_2$/water system, the XRD results revealed a noticeable feature that may benefit the photovoltaic property: the amount of unconverted PbI_2 was minimised. To qualitative express the conversion of $MAPbI_3$, we define the conversion of $MAPbI_3$ (C_{MAPbI3}) in reaction 2 as

$$C_{MAPbI3} \equiv \frac{I_{12.7^\circ}}{I_{12.7^\circ} + I_{14.2^\circ}}$$

where I is the intensity of the defined diffraction peak in Fig.3a. The correlation between C_{MAPbI3} and the MAI incubation time is showed in Fig. 3b. When the MAI incubation time increased, C_{MAPbI3} increased to 69.7% until 500 seconds, approximately the same percentage as that when $MAPbI_3$ was fabricated using the PbI_2/DMF system and 100 seconds of MAI incubation (blue dot, Fig. 3c). As mentioned previously and in published reports[30], the conversion of $MAPbI_3$ by using the PbI_2/DMF system is not complete because of an inevitable pristine PbI_2 residue. Interestingly, in the $Pb(NO_3)_2$/water system, the C_{MAPbI3} increased consistently and reached a plateau higher than 90% after 700 seconds of MAI incubation. To obtain deeper insights into $MAPbI_3$ crystal growth, the topographies of the XRD curves in Fig. 3a were scrutinised using SEM; Fig. 3c provides a summary. In the figure, the surface coverage of TiO_2 is imperfect owing to the islandish deposition of $Pb(NO_3)_2$ mentioned previously. A careful inspection of these images reveals that different crystal appearances during particular MAI incubation periods can be identified: sheet-like crystals in the early stage (100 seconds), various shapes of crystals containing irregular grains and thin rods in the intermediate stage (300–500 seconds), and thick rods and cuboid crystals in the final stage (after 700 seconds). According to XRD analysis, the formation of $MAPbI_3$ from $Pb(NO_3)_2$ can be classified into three stages: PbI_2, $MAPbI_3$-rich, and $MAPbI_3$-dominated phases. Integrating the information obtained from the

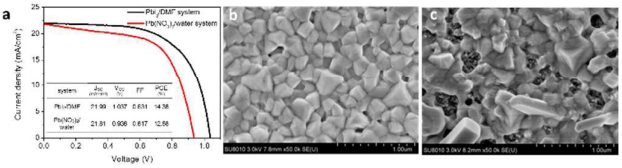

XRD and SEM analyses,

Fig. 4 J–V characteristics for the optimal cell and the morphology of $MAPbI_3$ layer created using the PbI_2/DMF and $Pb(NO_3)_2$/water systems. a, J–V curve for the optimal cell measured by averaging forward and reverse scan directions. b, SEM top-view image of $MAPbI_3$ layer created using the PbI_2/DMF system. c, SEM top-view image of $MAPbI_3$ layer created using the $Pb(NO_3)_2$/water system.

we speculate that the mechanism is as the follows: First, the $Pb(NO_3)_2$ reacts with MAI rapidly in an MAI solution and forms sheet-like PbI_2 crystals through ion displacement. Second, preferential nucleation of the $MAPbI_3$ at a particular facet results in lateral growth of crystals, changing the characteristic XRD pattern. Zoom-in images at 100 seconds and 200 seconds of the MAI incubation samples are provided in Figure S2, in which dramatic changes in crystal shapes, from sheet-like to irregular shapes, are apparent, verifying our speculation. Further crystal growth and an increasing volume during $MAPbI_3$ formation forces PbI_2/$MAPbI_3$ cocktails to merge, causing the irregular shape in the $MAPbI_3$-rich stage. Finally, large $MAPbI_3$ crystals tend to form cuboids or thick rods because of the long incubation duration[31, 32].

Figure 4 shows the photovoltaic performance of PSCs fabricated using $Pb(NO_3)_2$/water and PbI_2/DMF precursor systems and the corresponding top-view images of $MAPbI_3$-capped devices. In Fig. 4a, the current–voltage (J–V) curves of the optimally performing devices and their photovoltaic parameters are depicted in the table in the inset. The curves plotted in Fig. 4a are the averaged results of two scans from both sides. According to Fig. 4a, for the $Pb(NO_3)_2$/water system, the short-circuit photocurrent density (J_{SC}), open-circuit voltage (V_{OC}), and fill factor (FF) values derived from J–V curve are 21.81 mA/cm^2, 0.94 V, and 0.61 respectively, causing a PCE of 12.58% under one sun illumination. By comparison, PbI_2/DMF system yields a PCE of 14.38%, with a J_{SC} of 21.99 mA/cm^2, a V_{OC} of 1.04 V and an FF of 0.63. Although the PCE deviates by 1.8% when the aqueous $Pb(NO_3)_2$ precursor is used, Fig.4a indicates that the J_{SC} of the two devices is almost the same, revealing that the quality of the $MAPbI_3$ is nearly identical; the major difference in photovoltaic parameters of these two devices (V_{OC} and FF) is attributable to the morphology of the $MAPbI_3$ cap. Shown in Fig. 4b, the $MAPbI_3$ crystals appear as a capping layer that fully covers the TiO_2 scaffold in the PbI_2/DMF system, whereas the $MAPbI_3$ crystals fabricated using the $Pb(NO_3)_2$/water system failed to form a continuous capping film; thus, areas bare of TiO_2 are evident in Fig. 4c. The defect in the $MAPbI_3$ capping layer in the $Pb(NO_3)_2$/water system originates from the islandish deposition caused by spin-coating $Pb(NO_3)_2$, reflecting that the current film technology involving aqueous $Pb(NO_3)_2$ is far from perfect.

Nevertheless, our results confirm that using an aqueous lead source instead of a toxic DMF solvent is a viable method for fabricating high-purity perovskite crystals and highly efficient PSCs featuring a PCE exceeding two digits.

In summary, we developed a novel precursor combination for fabricating highly efficient PSCs by using an aqueous $Pb(NO_3)_2$ solution and created water-processed PSCs with a 12.58% PCE under standard conditions (AM1.5, 100 mW/cm^2). To the best of our knowledge, this is the first report of using water as processing solvent for PSCs. Eliminating the use of polar, toxic processing solvents such as DMF enables the feasibility of green production for PSCs. Moreover, we determined that the formation of $MAPbI_3$ from $Pb(NO_3)_2$ is a two-step reaction, proposing a possible mechanism involving the rapid formation of PbI_2 intermediates and the slow reaction of PbI_2 and MAI to form $MAPbI_3$. The inherent advantages of this process can be realised; for example, stoichiometrically controlling multi-halide perovskite becomes easy because the iodide no longer exists in the precursor, but rather exists in the MAI solution. The wettability between the substrate and $Pb(NO_3)_2$ during spin-coating is another concern; our UV-ozone treatment is effective but imperfect and requires improvement to enable a full-coverage coating. This study reveals that fabricating highly efficient PSCs by using a cost-effective, environmentally friendly process is promising.

This work was supported by Ministry of Science and Technology, Taiwan (MOST103-2221-E-007-121-MY2) and by a grant from the National Tsing-Hua University (104N2023E1). Financial support from Japan Science and Technology Agency (JST) Advanced Low Carbon Technology R&D program (ALCA) and Japanese Society for Promotion of Science (JSPS) Grant-in-Aid for Scientific Research B Grant Number 26289265 are also acknowledged.

Notes and references

1. A. Kojima, K. Teshima, Y. Shirai and T. Miyasaka, *Journal of the American Chemical Society*, 2009, **131**, 6050-6051.
2. J. H. Noh, S. H. Im, J. H. Heo, T. N. Mandal and S. I. Seok, *Nano letters*, 2013, **13**, 1764-1769.
3. K. Chondroudis and D. B. Mitzi, *Chemistry of materials*, 1999, **11**, 3028-3030.
4. Y. Lee, J. Kwon, E. Hwang, C. H. Ra, W. J. Yoo, J. H. Ahn, J. H. Park and J. H. Cho, *Advanced Materials*, 2015, **27**, 188-188.
5. M. M. Lee, J. Teuscher, T. Miyasaka, T. N. Murakami and H. J. Snaith, *Science*, 2012, **338**, 643-647.
6. H. Zhou, Q. Chen, G. Li, S. Luo, T.-b. Song, H.-S. Duan, Z. Hong, J. You, Y. Liu and Y. Yang, *Science*, 2014, **345**, 542-546.
7. N. J. Jeon, J. H. Noh, W. S. Yang, Y. C. Kim, S. Ryu, J. Seo and S. I. Seok, *Nature*, 2015, **517**, 476-480.
8. D. Liu, J. Yang and T. L. Kelly, *Journal of the American Chemical Society*, 2014, **136**, 17116-17122.
9. S. Aharon, B. E. Cohen and L. Etgar, *The Journal of Physical Chemistry C*, 2014, **118**, 17160-17165.
10. O. Malinkiewicz, A. Yella, Y. H. Lee, G. M. Espallargas, M. Graetzel, M. K. Nazeeruddin and H. J. Bolink, *Nature Photonics*, 2014, **8**, 128-132.
11. N. J. Jeon, J. H. Noh, Y. C. Kim, W. S. Yang, S. Ryu and S. I. Seok, *Nat Mater*, 2014, **13**, 897-903.
12. J. Burschka, N. Pellet, S.-J. Moon, R. Humphry-Baker, P. Gao, M. K. Nazeeruddin and M. Grätzel, *Nature*, 2013, **499**, 316-319.
13. J.-H. Im, I.-H. Jang, N. Pellet, M. Grätzel and N.-G. Park, *Nature nanotechnology*, 2014, **9**, 927-932.
14. C. W. Chen, H. W. Kang, S. Y. Hsiao, P. F. Yang, K. M. Chiang and H. W. Lin, *Advanced Materials*, 2014, **26**, 6647-6652.
15. Y. Wu, A. Islam, X. Yang, C. Qin, J. Liu, K. Zhang, W. Peng and L. Han, *Energy & Environmental Science*, 2014, **7**, 2934-2938.
16. K. Yan, M. Long, T. Zhang, Z. Wei, H. Chen, S. Yang and J. Xu, *Journal of the American Chemical Society*, 2015, **137**, 4460-4468.
17. W. Zhang, M. Saliba, D. T. Moore, S. K. Pathak, M. T. Hörantner, T. Stergiopoulos, S. D. Stranks, G. E. Eperon, J. A. Alexander-Webber and A. Abate, *Nature communications*, 2015, **6**.
18. F. K. Aldibaja, L. Badia, E. Mas-Marza, R. S. Sanchez, E. M. Barea and I. Mora-Sero, *Journal of Materials Chemistry A*, 2015, **3**, 9194-9200.
19. F. Wang, H. Yu, H. Xu and N. Zhao, *Advanced Functional Materials*, 2015, **25**, 1120-1126.
20. G. Balaji, P. H. Joshi, H. A. Abbas, L. Zhang, R. Kottokkaran, M. Samiee, M. Noack and V. L. Dalal, *Physical Chemistry Chemical Physics*, 2015, **17**, 10369-10372.
21. M. Grätzel, *Nature materials*, 2014, **13**, 838-842.
22. F. Hao, C. C. Stoumpos, D. H. Cao, R. P. Chang and M. G. Kanatzidis, *Nature Photonics*, 2014, **8**, 489-494.
23. N. K. Noel, S. D. Stranks, A. Abate, C. Wehrenfennig, S. Guarnera, A.-A. Haghighirad, A. Sadhanala, G. E. Eperon, S. K. Pathak and M. B. Johnston, *Energy & Environmental Science*, 2014, **7**, 3061-3068.
24. M. H. Kumar, S. Dharani, W. L. Leong, P. P. Boix, R. R. Prabhakar, T. Baikie, C. Shi, H. Ding, R. Ramesh and M. Asta, *Advanced Materials*, 2014, **26**, 7122-7127.
25. P. P. Boix, S. Agarwala, T. M. Koh, N. Mathews and S. G. Mhaisalkar, *The Journal of Physical Chemistry Letters*, 2015, **6**, 898-907.
26. J.-D. Wang, M.-Y. Lai, J.-S. Chen, J.-M. Lin, J.-R. Chiang, S.-J. Shiau and W.-S. Chang, *Archives of Environmental Health: An International Journal*, 1991, **46**, 161-166.
27. L. E. Fleming, S. L. Shalat and C. A. Redlich, *Scandinavian journal of work, environment & health*, 1990, 289-292.
28. D. T. Moore, H. Sai, K. W. Tan, L. A. Estroff and U. Wiesner, *APL Materials*, 2014, **2**, 081802.
29. G. Balaji, P. H. Joshi, H. A. Abbas, L. Zhang, R. Kottokkaran, M. Samiee, M. Noack and V. L. Dalal, *Physical Chemistry Chemical Physics*, 2015, **17**, 10369-10372.
30. A. Wakamiya, M. Endo, T. Sasamori, N. Tokitoh, Y. Ogomi, S. Hayase and Y. Murata, *Chem. Lett*, 2014, **43**, 711-713.
31. D. H. Cao, C. C. Stoumpos, C. D. Malliakas, M. J. Katz, O. K. Farha, J. T. Hupp and M. G. Kanatzidis, *APL Materials*, 2014, **2**, 091101.
32. W. Chen, Y. Wu, J. Liu, C. Qin, X. Yang, A. Islam, Y.-B. Cheng and L. Han, *Energy & Environmental Science*, 2015, **8**, 629-640.